Article

Solar Thermochemical CO₂ Splitting Integrated with Supercritical CO₂ Cycle for Efficient Fuel and Power Generation

Xiangjun Yu [1], Wenlei Lian [1,2,*], Ke Gao [1], Zhixing Jiang [1], Cheng Tian [1], Nan Sun [1], Hangbin Zheng [1], Xinrui Wang [1], Chao Song [1] and Xianglei Liu [1,2]

[1] School of Energy and Power Engineering, Nanjing University of Aeronautics and Astronautics, Nanjing 210016, China
[2] Integrated Energy Institute, Nanjing University of Aeronautics and Astronautics, Nanjing 210016, China
* Correspondence: wenlian@nuaa.edu.cn

Abstract: Converting CO_2 into fuels via solar-driven thermochemical cycles of metal oxides is promising to address global climate change and energy crisis challenges simultaneously. However, it suffers from low energy conversion efficiency (η_{en}) due to high sensible heat losses when swinging between reduction and oxidation cycles, and a single product of fuels can hardly meet multiple kinds of energy demands. Here, we propose an alternative way to upsurge energy conversion efficiency by integrating solar thermochemical CO_2 splitting with a supercritical CO_2 thermodynamic cycle. When gas phase heat recovery (ε_{gg}) is equal to 0.9, the highest energy conversion efficiency of 20.4% is obtained at the optimal cycle high pressure of 260 bar. In stark contrast, the highest energy conversion efficiency is only 9.8% for conventional solar thermochemical CO_2 splitting without including a supercritical CO_2 cycle. The superior performance is attributed to efficient harvesting of waste heat and synergy of CO_2 splitting cycles with supercritical CO_2 cycles. This work provides alternative routes for promoting the development and deployment of solar thermochemical CO_2 splitting techniques.

Keywords: cerium dioxide; concentrated solar; solar fuel; thermochemical cycle; thermodynamic analysis

1. Introduction

Concentrations of carbon dioxide in the atmosphere have been continuously increasing by 50% since the beginning of the industrial era and set a new record value of 421 ppm in 2022 [1]. Unprecedented CO_2 has led to severe climate change and global warming problems, which threatens the sustainable development of human beings. The dominant contribution of excess CO_2 emissions is related with massive utilization of fossil fuels. Employing sustainable energy to convert CO_2, the major products of carbon-containing fuels combustion, into fuels such as carbon monoxide (CO) is one of the most effective routes to reduce CO_2 concentrations [2]. On the other hand, CO is one of the main components of syngas, which can be further converted into liquid fuels through the Fischer-Tropsch process [3–5]. Therefore, converting CO_2 into fuels is promising to tackle both climate change problems by reducing CO_2 in the atmosphere and energy crisis challenges via providing sustainable carbon fuels.

Several methods of using solar energy to produce CO are on the list. Photocatalysis [5–8], electrolysis [9–11], and thermochemical CO_2 splitting [12–14] have been investigated extensively. Recently, thermochemical CO_2 splitting has attracted widespread attention due to its high theoretical energy conversion efficiency (η_{en}) due to the capability of utilizing the entire solar spectrum [15–17]. For one-step CO_2 decomposition, an extremely high temperature over 3000 K is required [18], and mixture gas (possible explosive) needs to be separated, which consumes extra energy. Two-step non-volatile metal oxide cycles, on the other hand, can reduce the required decomposition temperature down to 1773 K and

produce O_2 and CO in separate steps [19], thus avoiding energy-consuming gas separation issues. Meanwhile, metal oxide cycles enable rather simple design and operation and can achieve high solar-to-fuel efficiency theoretically [20–22]. The process of two-step metal oxide cycles is shown as Equations (1)–(3),

$$M_xO_{y-\delta_{ox}} \rightarrow M_xO_{y-\delta_{red}} + \Delta\delta/2 O_2 \qquad (1)$$

$$M_xO_{y-\delta_{red}} + \Delta\delta CO_2 \rightarrow M_xO_{y-\delta_{ox}} + \Delta\delta CO \qquad (2)$$
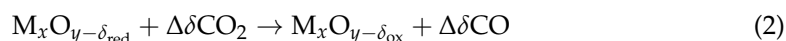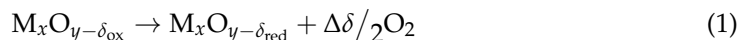
$$\Delta\delta = \delta_{red} - \delta_{ox} \qquad (3)$$

where $M_xO_{y-\delta_{red}}$ and $M_xO_{y-\delta_{ox}}$ represent the reduced and oxidized metal oxides, respectively. $\Delta\delta = \delta_{red} - \delta_{ox}$ is the nonstoichiometric swing of the redox material between the reduced and oxidized states.

To achieve a high solar-to-fuel efficiency, developing new materials and optimizing cyclic systems have been extensively investigated in a parallel effort. Ceria has been investigated from a wide range of oxygen pressures and temperatures due to its rapid reaction kinetics at high temperatures [23]. On this basis, the transition metals such as Ca^{2+}, Cr^{3+} and Zr^{4+} were doped into cerium dioxide to further increase the CO yield to 156, 251, and 315.4 µmol/g, respectively [24–26]. Recently, perovskite oxides have received much attention due to their lower reaction temperatures and high CO yield. Gao et al. reported a high CO yield of 595.6 µmol/g based on $Sm_{0.6}Ca_{0.4}Mn_{0.8}Al_{0.2}O_3$ [27]. Different reactor designs are also investigated to achieve high efficiencies. For example, researchers proposed a rotary-type reactor by using the reactive ceramics of ceria and $Ni_{0.5}Mn0_{.5}Fe_2O_4$ to produce CO continuously, and the highest average efficiency of 0.66% was obtained [28,29]. Marxer et al. designed a high-temperature solar reactor containing a reticulated porous ceramic, which was made of pure ceria, and obtained a maximum solar-to-fuel efficiency of 1.73% [30]. Haeussler et al. designed and tested a monolithic solar reactor using cerium dioxide foam with a peak solar fuel efficiency higher than 8% [2]. However, energy conversion efficiency based on traditional metal oxide cycles is still limited due to high sensible heat losses when switching between reduction and oxidation processes. Such heat losses can be harvested via a high-temperature particle-particle heat exchanger but suffer from low efficiencies due to a poor heat transfer coefficent between particles. In addition, the single product of fuels can hardly meet multiple kinds of energy demands for practical applications.

In this paper, we propose to combine thermochemical CO_2 splitting with a supercritical CO_2 Bryton cycle and to use cerium dioxide as an intermediate medium. The heat dissipated by cerium dioxide from a high reduction temperature down to a low oxidation temperature is used to heat the supercritical CO_2, which is then fed to the turbine to export power. Simultaneously, cerium dioxide is oxidized at low temperatures to produce CO, which can be used as solar fuel. This combined cycle enriches products of traditional thermochemical CO_2 splitting cycles and makes it possible to reach a higher overall energy efficiency of 20.4% compared with 9.8% otherwise. More detailed thermodynamic analysis and economic analysis, including the energy distribution of sub-systems and effects of different operating parameters on the system efficiency, are discussed.

2. Thermodynamic Model

The system of combining a solar thermochemical CO_2 splitting system [31,32] and a supercritical CO_2 Brayton cycle [33,34] is shown in Figure 1, in which ceria is used as intermediate medium to transport energy. Sunlight ($I = 1$ kW/m^{-2}) shines directly on the heliostat which concentrates solar energy into the solar receiver via reflection. Cerium dioxide particles are irradiated directly by sunshine inside the solar receiver and are rapidly heated to reduction temperature to release O_2. The solar receiver is maintained at a low pressure using a vacuum pump to ensure that the cerium dioxide reduction reaction continues. O_2 cleaved from the fluorite phase is removed by the vacuum pump. Meanwhile, CO_2 enters the compressor at room temperature (T_0) and is compressed to

circulating high pressure (P_7), passing through a heat exchanger at the turbine outlet to reach an intermediate temperature (T_8), and then flows into the reaction chamber. In the reaction chamber, CO_2 and ceria exchange heat and undergo an oxidation reaction, during which CO is produced. Therefore, the CO_2 flowing out of the reaction chamber also contains CO, which will be split up by the separator. The pure CO_2 leaves the separator and enters the turbine to expand and export power and then flows into the heat exchanger to recover the waste heat.
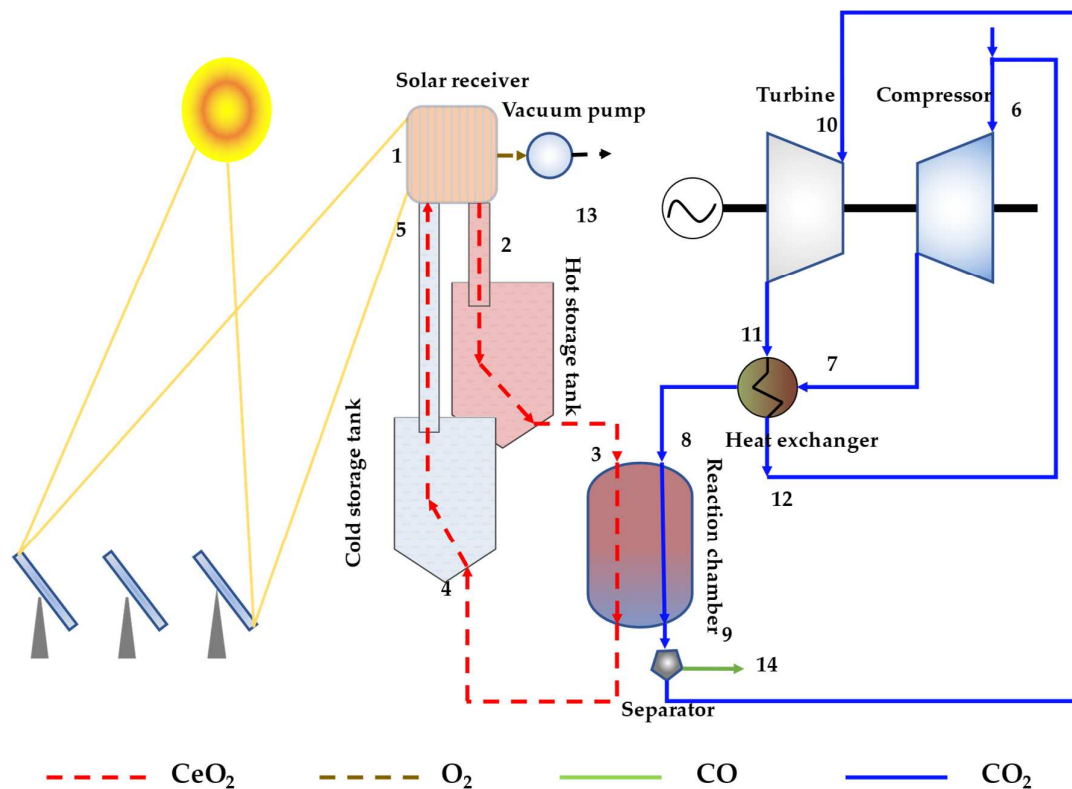
Figure 1. Schematic diagram of ceria-based solar thermochemical CO_2 splitting system integrated with a supercritical CO_2 Brayton cycle.

It is noted that the functions given require temperatures in Kelvin and pressures in bar for a uniform form of expression. We assume that the system operates in steady-state and thermodynamic equilibrium, meaning that all heat and mass fluxes are independent of time. This facilitates us to calculate the optimal energy conversion efficiency of the system, since the continuous production avoids the start-up and cooling process of the material, thus minimizing losses.

2.1. Thermodynamic Efficiency

We introduce thermodynamic efficiency (η_{th}) to calculate energy uniformly, which depends on the energy obtained by solar receiver ($\dot{Q}_{\text{rec}}$), radiation loss ($\dot{Q}_{\text{rad}}$), convection loss ($\dot{Q}_{\text{conv}}$), and reflected energy ($\dot{Q}_{\text{ref}}$). The energy analysis of the fixed heliostat field and the solar receiver is shown below. The design parameters are shown in Table 1 as well.

$$\dot{Q}_{\text{rec}} = \eta_{\text{h}} IC \tag{4}$$

where *I* is the direct normal solar irradiation intensity, *C* is the solar concentration ratio, and η_{h} is the optical efficiency. It is noted that optical efficiency varies widely depending on specific designs, taking values from 60% [35] to 90% [36,37]. Since the decrease in optical

efficiency suppresses the overall system efficiency, we choose the upper value of the interval to maximize the energy conversion efficiency.

The radiation and convection loss rates of the solar receiver are represented by Equations (5) and (6), respectively [38,39],

$$\dot{Q}_{\text{rad}} = A_{\text{ape}} \varepsilon \sigma (T_{\text{surf}}{}^4 - T_0{}^4) \tag{5}$$

$$\dot{Q}_{\text{conv}} = h_{\text{nc}} (T_{\text{surf}} - T_0) A_{\text{surf}} + h_{\text{fc}} (T_{\text{surf}} - T_0) A_{\text{ape}} \tag{6}$$

where A_{ape} is the receiver aperture size, A_{surf} is the surface area of the receiver, ε is the average emissivity of the solar receiver ($\varepsilon = 0.85$), and σ is the Stefan–Boltzmann constant. The convection loss of the solar receiver is the sum of the forced convection loss and the natural convection loss. The forced convection loss comes from the flat plate and is related to the size of the aperture. The natural convection cavity is similar to the flat plate. Here, the wall temperature (T_{surf}) of the receiver is 20 K higher than the reduction temperature (T_1) [39,40]. We noted that there is a critical point for supercritical CO_2 (7.38 Mpa, 304 K), so here, we set T_0 to 305K [41].

Since the solar receiver reflectivity changes with surface temperature, the numerical simulation of reflection loss is difficult to implement. Therefore, we introduce the view factor with reflectance to simplify the calculation

$$\dot{Q}_{\text{ref}} = \dot{Q}_{\text{rec}} \rho F_{\text{r}} \tag{7}$$

wherein ρ is the reflectance and F_{r} is the view factor. The view factor is defined as the ratio of the solar receiver aperture area to the solar receiver surface area [42].

According to the first law of thermodynamics, the remaining absorbed heat can be computed as:

$$\dot{Q}_{\text{abs}} = \eta_{\text{h}} IC - \dot{Q}_{\text{rad}} - \dot{Q}_{\text{conv}} - \dot{Q}_{\text{ref}} \tag{8}$$

The thermodynamic efficiency thus can be counted due to the analysis of heat loss from Equation (9).

$$\eta_{\text{th}} = \frac{\eta_{\text{h}} IC - \dot{Q}_{\text{rad}} - \dot{Q}_{\text{conv}} - \dot{Q}_{\text{ref}}}{IC} \tag{9}$$

Table 1. Properties and values for the integrated system.

Property	Value(s)
C	3000
F_{r}	0.0757
T_{red}	1400–2100 K
T_{ox}	700–1500 K
P_0	1 bar
$P_{\text{c,in}}$	72–90 bar
$P_{\text{t,in}}$	180–300 bar
η_{mech}	0.1
$\eta_{\text{O2-rem}}$	0.15
η_{sep}	0.15
ρ	0.05

2.2. Ceria's Reduction and Heating

We set T_1 as the reduction temperature (T_{red}) and T_4 as the oxidation temperature (T_{ox}) to describe the loop conveniently. Equations (1) and (2) describe the cyclic reaction of cerium dioxide. Ceria is reduced in a low oxygen atmosphere at a temperature of T_1 and a partial pressure of oxygen, P_{red}. δ_{red} is the oxygen vacancy concentration after reduction reaction. Cerium dioxide is then oxidized in CO_2 at a pressure of P_{ox}, where the oxygen

vacancy concentration is δ_{ox}. The yield of each cycle is the difference in oxygen vacancy concentration $\Delta\delta$. For ease of understanding, δ is defined as a unitless measure:

$$\delta = \frac{[O]}{[Ce]} \tag{10}$$

where [O] is the concentration of oxygen vacancies and [Ce] is the concentration of cerium atoms.

Factors affecting the oxygen vacancy concentration of cerium dioxide have long been the subject of research [23,43]. After continuous exploration, it has been found that the oxygen vacancy concentration is only related to the temperature and the amount of oxygen pressure in the environment. The properties of cerium dioxide have also been investigated over a wide range of oxygen partial pressures (10^{-2} to 10^{-8} bar) and temperatures (1273–2173 K) [44]. Bulfin et al. fitted the curve based on the accumulated experimental data and obtained Equation (11) [44].

$$\left(\frac{\delta}{0.35 - \delta}\right) = 8700 P_{O_2}{}^{-0.217} \exp\left(\frac{-195.6 \text{ kJ mol}^{-1}}{RT}\right) \tag{11}$$

The units of temperature in Equation (11) are Kelvin and the units of partial pressure of oxygen are bar. We bring T_1 into Equation (11) with the adjusted oxygen partial pressure P_{red} in the solar receiver to calculate δ_{red}. For calculating δ_{ox}, the oxygen partial pressure in T_4 and 200 bar CO_2 is brought into Equation (11), where parameters used in the calculation of δ_{ox} are computed via HSC.

Figure 2 shows the values of nonstoichiometric coefficient δ in a low oxygen partial pressure and a CO_2 atmosphere. The δ_{red} and δ_{ox} we calculate are consistent with previous thermodynamic studies [45]. Meanwhile, cerium dioxide requires energy (ΔH_{red}) to undergo reduction to remove the oxygen atoms from the lattice. The change in enthalpy has been found to only depend on the nonstoichiometric coefficient [23]. A polynomial curve of the enthalpy change was fitted.

$$\Delta H = (478 - 1158\delta + 1790\delta^2 + 23368\delta^3 - 64929\delta^4)10^3 \tag{12}$$

The heat required to reduce 1 mol of cerium dioxide from δ_{red} to δ_{ox} can be obtained via variable integration using Equation (12). However, oxidizing cerium dioxide to δ_{red} requires an excess of oxidant. Therefore, we introduce a stopping point for the oxidation reaction:

$$\delta_{ox}(\alpha) = \delta_{ox} + (1 - \alpha)\Delta\delta, \quad 0 < \alpha < 1 \tag{13}$$

where α is the fraction of the reaction completed and is a number between 0 and 1. Based on a previous calculation [46,47], we take the value of α to be 0.95. Combining Equations (12) and (13), the energy required for the reduction of cerium dioxide can be counted.

$$\dot{Q}_{red} = \dot{n}_{CeO_2} \int_{\delta_{ox}(\alpha)}^{\delta_{red}} \Delta H \, d\delta \tag{14}$$

Since the re-oxidation process of cerium dioxide involves the decomposition of CO_2 and the generation of CO, the energy ($\dot{Q}_{HOX}$) required for the oxidation of cerium dioxide can be obtained according to the empirical formula [22]

$$\dot{Q}_{hox} = \dot{n}_{CeO_2}\left(-\Delta H_{red} - \Delta H^f_{CO_2} + \Delta H^f_{CO}\right) \tag{15}$$

where ΔH_{red} represents the heat required for 1 mol of cerium dioxide to be reduced, and this can be calculated using Equations (12) and (13). The $\Delta H^f_{CO_2}$ and ΔH^f_{CO} are the mole heat of the formation of CO_2 and CO, respectively, which can be found from the NIST Chemistry Webbook.
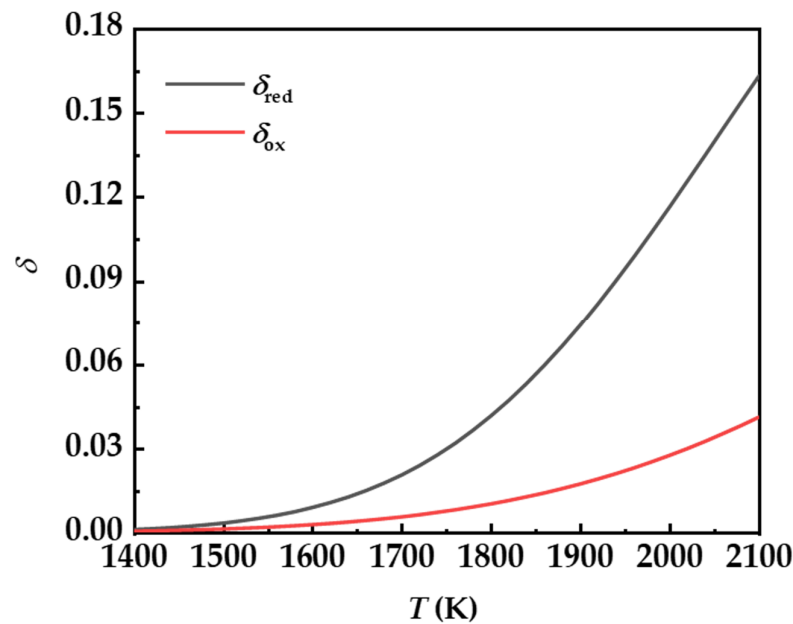
Figure 2. Nonstoichiometric coefficient,δ_{red}, as a function of temperature, T, for a reduction with $P_{O_2} = 10^{-4}$ bar. δ_{ox} as a function of T, for an oxidation with $P_{CO_2} = 200$ bar.

Ceria will be heated from T_4 to T_1 after entering the solar receiver. The heat capacity for ceria is taken to be 80 J/mol K [48], because the specific capacity heat of ceria dioxide has little change in the range of 1400–2100 K.

$$\dot{Q}_{CeO_2} = \dot{n}_{CeO_2} Cp_{CeO_2}(T_4 - T_1) \tag{16}$$

The heat ($\dot{Q}_{reco}$) recovered from the reheater at the outlet of the turbine is used to heat more supercritical CO_2. Although this heat is not counted as solar energy, it is also one of the energy sources worth investigating.

$$\dot{Q}_{reco} = \dot{n}_{CO_2,t,out} \varepsilon_{gg}(h_{11} - h_{12}) = \dot{n}_{CO_2}(h_8 - h_7) \tag{17}$$

The local heat capacity of supercritical CO_2 varies greatly, thus, the return heat exchanger is generally of segmented design [49], and discontinuous design allows for faster heat transfer [50]. For the convenience of calculation, we use ε_{gg} to denote the heat transfer efficiency of the return heater.

2.3. Storage Tank and Reaction Chamber

Cerium dioxide pellets are transported to a hot tank for storage and subsequently enter the reaction chamber to exchange heat with CO_2 and react. Both components have heat losses to the environment, so we discuss them together. The main sources of energy loss in a particle storage facility are convection from the surrounding environment and conduction from the bin walls [51], which can be expressed by Equation (18).

$$\dot{Q}_{loss,tank} = \dot{Q}_{foundation} + \int_0^l ph\left(T_{tank} - T_0\right) dx + \dot{Q}_{top} \tag{18}$$

$$\dot{Q}_{loss,tank} = \dot{n}_{CeO_2} Cp_{CeO_2}(T_2 - T_3) \tag{19}$$

where $\dot{Q}_{foundation}$ and $\dot{Q}_{top}$ are the heat loss at the bottom and top of the heat storage tank, respectively. The perimeter p is for a round silo to $2\sqrt{\pi A}$, and A is the silo cross sectional area. The heat loss of the silo is integrated along the silo height l. According to

the second law of thermodynamics, the outlet temperature of the heat storage tank can be easily calculated using Equation (19).

In the reaction chamber, cerium dioxide reacts with CO_2 in an oxidation process and heat exchange takes place. This can be achieved using either a fluidized bed or a cyclone heat exchanger [52,53]. In order to facilitate the calculations, the pressure drop in the reaction chamber is ignored and the forced heat balance is reached at the outlet.

$$\dot{Q}_{\text{loss,camber}} + \dot{n}_{\text{CeO}_2}\left(h_3 - h_4\right) + \dot{Q}_{\text{hox}} = \dot{n}_{\text{CO}_2}\left(h_9 - h_8\right) + \dot{n}_{\text{CO}}HHV \tag{20}$$

The energy that can be released by the fuel is expressed in terms of the high heat value (*HHV*), because CO is gaseous and there is no latent heat of vaporization. Thus, here, the *HHV* is equal to the value of the low heat value (i.e., heat of combustion).

2.4. Auxiliary Energy

In exception to chemical reactions that require heat to complete the reaction, the system requires additional energy to complete the cycle, including removal of oxygen from the solar receiver ($\dot{Q}_{\text{pump}}$), transport of cerium dioxide between cold/hot tanks ($\dot{Q}_{\text{mech}}$), compression of supercritical CO_2 from low to high pressure in the cycle ($\dot{W}_{\text{c}}$), and separation of the mixture of CO_2 and CO ($\dot{Q}_{\text{sep}}$).

Other methods such as inert gas sweeping and chemical removal can remove the generated oxygen [54]; here, we use a vacuum pump to remove the excess oxygen in the solar receiver for convenience of calculation and give the formula

$$\dot{Q}_{\text{pump}} = \dot{n}_{\text{O}_2}RT_0\ln\left(\frac{P_0}{P_{\text{red}}}\right)\frac{1}{\eta_{\text{pump}}} \tag{21}$$

wherein the value of P_{red} is equal to the partial pressure of oxygen at point 1 and the pumping efficiency (η_{pump}) is as shown in Table 1.

The particles in the thermochemical CO_2 splitting system need to be transported to the solar receiver and sent to the thermal storage tank for cycling. We assume that the transport height H for one cycle is 10 m. The mechanical work is obtained by dividing the gravitational potential energy by the mechanical efficiency (η_{mech}). The energy share of $\dot{Q}_{\text{mech}}$ in the system is very low (less than 1%) and almost negligible.

$$\dot{Q}_{\text{mech}} = \dot{n}_{\text{CeO}_2}\frac{M \times g \times H}{\eta_{\text{mech}}} \tag{22}$$

In a supercritical CO_2 Brayton cycle, the compressor works on the same principle as a turbine, in which CO_2 is compressed or expanded, resulting in a change in enthalpy that can be calculated as power. The flow rate in the compressor and the turbine is not the same due to the fact that the CO_2 flows through the separator and into the turbine.

$$\dot{W}_{\text{c}} = \dot{n}_{\text{CO}_2}\left(h_7 - h_6\right) \tag{23}$$

$$\dot{W}_{\text{t}} = \dot{n}_{\text{CO}_2,\text{t,in}}\left(h_{10} - h_{11}\right) \tag{24}$$

The energy required for the separator can be determined using the second law of thermodynamics with the entropy of the separated gas divided by the separation efficiency (η_{sep}) to derive Equation (25). Here, $\dot{n}_{\text{mix}}$ and ΔS_{mix} correspond to the flow rate and the entropy of the unseparated gas mixture at state 9, respectively. We assume that the value of T_{sep} is equal to the oxidation temperature.

$$\dot{Q}_{\text{sep}} = \frac{\Delta S_{\text{unmix}}T_{\text{sep}}}{\eta_{\text{sep}}} = T_{\text{sep}}\left(\dot{n}_{\text{CO}}\Delta S_{14} + \dot{n}_{\text{CO}_2,\text{sep,out}}\Delta S_{10} - \dot{n}_{\text{mix}}\Delta S_{\text{mix}}\right)\frac{1}{\eta_{\text{sep}}} \tag{25}$$

2.5. System Efficiency

The total amount of energy essential for the operation of a ceria-based thermochemical CO_2 splitting system integrating supercritical CO_2 is computed via Equation (26).

$$\dot{Q}_{tc} = \dot{Q}_{CeO_2} + \dot{Q}_{red} + \dot{Q}_{pump} + \dot{Q}_{mech} + \dot{Q}_{sep} + \dot{W}_{c} \tag{26}$$

Based on our calculated thermodynamic efficiency, we can work out the solar energy needed for the system.

$$\dot{Q}_{solar} = \frac{\dot{Q}_{tc}}{\eta_{th}} \tag{27}$$

The total energy losses of the system are also computed using Equation (28).

$$\dot{Q}_{loss} = \dot{Q}_{solar}(1 - \eta_{th}) \tag{28}$$

The system fuel efficiency (η_{fuel}) of the process is defined as the ratio of the high heating value of the production fuel to the solar energy needed to drive the cycle. Analogously, the system's turbine efficiency (η_{W_t}) can be defined as the ratio of power exported by the turbine to the total solar energy.

$$\eta_{fuel} = \frac{\dot{n}_{CO}HHV}{\dot{Q}_{solar}} \tag{29}$$

$$\eta_{W_t} = \frac{\dot{W}_t}{\dot{Q}_{solar}} \tag{30}$$

To count the energy conversion of the system, we write Equation (31) by adding the values of η_{fuel} and η_{W_t}.

$$\eta_{en} = \frac{\dot{n}_{CO}HHV + \dot{W}_t}{\dot{Q}_{solar}} \tag{31}$$

3. Results

3.1. Oxygen Partial Pressure during Reduction

In terms of the degree of δ_{red} created in the ceria crystal structure, Figure 3a reports the amount of O_2 released during reduction conducted at different T_{red} (from 1400–2100 K) and P_{red} (from 10^{-3}–10^{-5} bar). The results presented show that, at all T_{red}, the δ_{red} upsurged with the reduction in the P_{red}. For instance, the δ_{red} was increased by 0.077, 0.037, 0.009, and 0.001 at 2100 K, 1900 K, 1700 K, and 1500 K, respectively, when the P_{red} was decreased from 10^{-3}–10^{-5} bar. Simultaneously, the growth in the T_{red} was beneficial towards improving the capacity of O_2 released during reduction. In terms of values, the δ_{red} was increased by 0.12, 0.16, and 0.21 when the T_{red} was enhanced from 1400–2100 K at stable $P_{red} = 10^{-3}$ bar, $P_{red} = 10^{-4}$ bar, and $P_{red} = 10^{-5}$ bar, separately.

The effect of T_{red} on $\dot{n}_{CO_2}$, $\dot{n}_{CO_2,sep,out}$, and $\dot{n}_{CO,sep,out}$ is shown in Figure 3b. The $\dot{n}_{CO_2}$ and the $\dot{n}_{CO_2,sep,out}$ were reduced due to the increment in the $\dot{Q}_{loss}$. For example, as the T_{red} was upsurged from 1400–2100 K, the $\dot{n}_{CO_2}$ and $\dot{n}_{CO_2,sep,out}$ decreased by 16.7 mol/s and 17.9 mol/s, respectively. On the contrary, the $\dot{n}_{CO,sep,out}$ rose by 1.3 mol/s due to the escalation in the T_{red} from 1400–2100 K. The variations in the $\dot{W}_t$, $\dot{n}_{CO}HHV$, and $\dot{Q}_{solar}$ due to the decrease of P_{red} are presented in Figure 3c. As the released O_2 was increased due to the decreased P_{red} from 10^{-3} to 10^{-5} bar, a greater quantity of CO was produced during the oxidation reaction, i.e., the $\dot{n}_{CO}HHV$ rose from 307.6–508.9 kW at 1900 K. In contrast, the $\dot{W}_t$ decreased from 138.1–107.0 kW due to the upsurged CO when the P_{red} decreased from 10^{-3}–10^{-5} bar. In terms of numbers, the value and growth of $\dot{n}_{CO}HHV$ far exceeds

that of $\dot{W}_t$. Simultaneously, the $\dot{Q}_{solar}$ was increased from 3680.4–4048.6 kW due to the increment in the P_{red} from 10^{-3} to 10^{-5} bar.

The efficiency analysis was initiated by exploring the effect of oxygen partial pressure (P_{red}) on the various process parameters at constant T_{ox} = 1300 K, $P_{c,in}$ = 75 bar, and $P_{t,in}$ = 200 bar. By using Equation (31), the η_{en} was computed. As shown in Figure 3d, the numbers obtained indicated that each curve of η_{en} had a peak at high temperatures at all P_{red} as the T_{ox}, $P_{c,in}$, and $P_{t,in}$ were kept constant. All these peak values were observed to be increased with the increased P_{red}. In terms of numerical values, the value of the peak escalated from 12.2–15.2%, and the peak temperatures went down from 1950–1850 K due to the decrease in the P_{red} from 10^{-3}–10^{-5} bar.
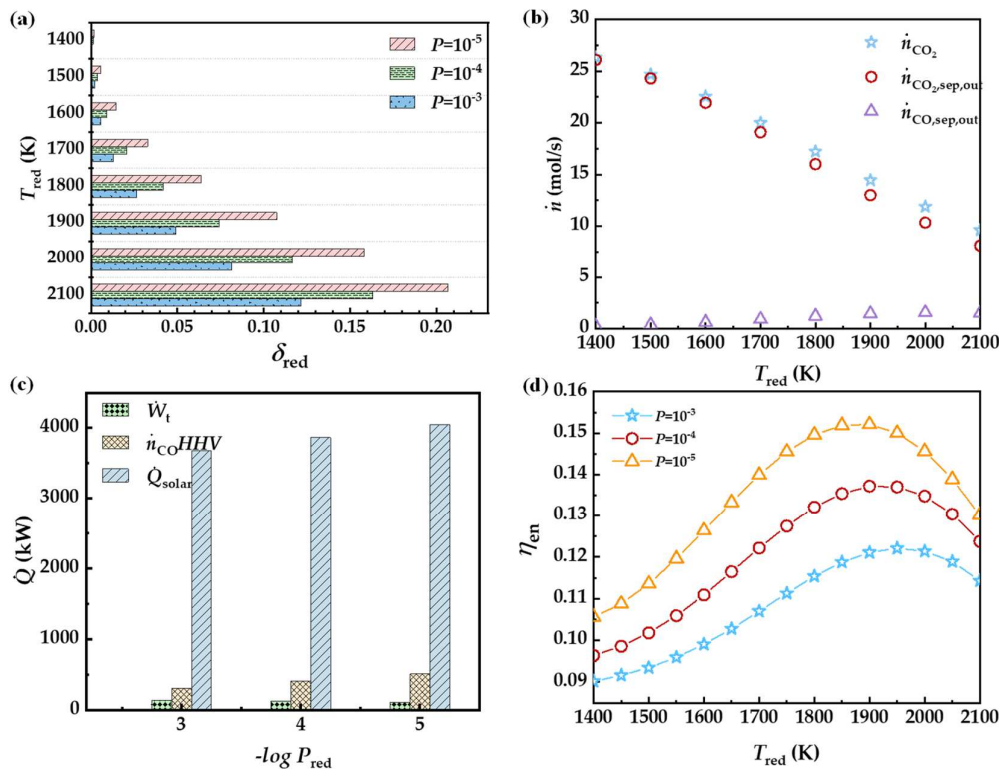
Figure 3. (**a**) Effect of P_{red} and T_{red} on δ_{red} of ceria, (**b**) influence of T_{red} on $\dot{n}_{CO_2}$, $\dot{n}_{CO_2,sep,out}$, and $\dot{n}_{CO,sep,out}$ (P_{red} = 10^{-4} bar), (**c**) effect of P_{red} on $\dot{W}_t$, $\dot{n}_{CO}HHV$, and $\dot{Q}_{solar}$ (T_{red} = 1900 K), (**d**) influence of T_{red} on η_{en} (T_{ox} = 1300 K, P_{red} = P, α = 0.95, ε_{gg} = 0, $P_{c,in}$ = 75 bar, and $P_{t,in}$ = 200 bar).

3.2. Reduction Temperature

In this part, the effect of oscillation in the T_{red} from 1400–2100 K at constant P_{red} = 10^{-4} bar and T_{ox} = 1300 K on the energy distribution of the cycle was examined. Firstly, the values associated with η_{th} were computed using Equation (9). As the T_{ox} was steady at 1300 K, the η_{th} was reduced by 33% due to the rise in the T_{red} from 1400–2100 K.

Figure 4b shows the percentage of energy required for each part of the system. The heat losses due to radiation, convection, and reflection were estimated as Equations (5)–(7). As expected according to the principles of heat transfer, $\dot{Q}_{loss}$ was observed to be increased with the rise in T_{red}. For instance, as the T_{red} rose from 1400–2100 K, the percentage of $\dot{Q}_{loss}$ upsurged from 0.26–0.59. Meanwhile, with the increase of T_{red}, a higher quantity of O_2 was released. Thus, as the δ_{red} upsurged, the energy needed to drive the reduction reaction also increased considerably. In terms of ratios, when the $\dot{Q}_{rec}$ was constant and the T_{red} was increased from 1400–2100 K, the proportion of $\dot{Q}_{CeO_2}$ decreased from 0.67–0.16 because of the increased $\dot{Q}_{loss}$ and $\dot{Q}_{red}$. In contrast, the ratio of $\dot{Q}_{red}$ increased from 0.03–0.18 when T_{red} upsurged from 1400–2000 K, due to the rise in the conversion rate, and decreased by

0.02 as T_{red} was 2100 K because of the increment of $\dot{Q}_{loss}$. The summary of $\dot{Q}_{mech}$, $\dot{Q}_{pump}$, $\dot{Q}_{sep}$, and $\dot{W}_c$ accounted for 0.04 of $\dot{Q}_{solar}$ when the T_{red} was 1400 K, and the proportion rose to 0.09 as the T_{red} reached 2100 K. The change in proportion in this process was tiny enough to be ignored.

(a)

(b)
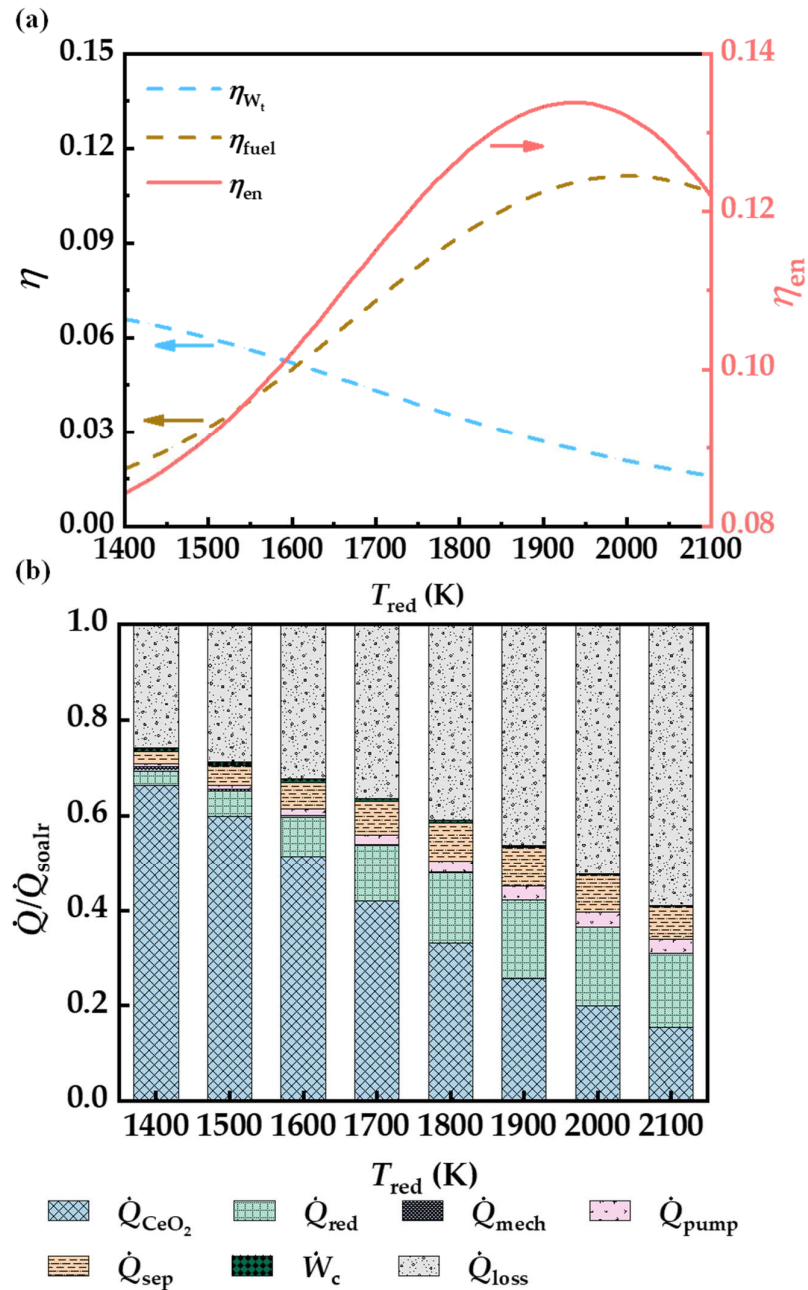
Figure 4. (a) Effect of T_{red} on η_{fuel}, η_{W_t}, and η_{en} ($P_{red} = 10^{-4}$ bar), (b) energy balance chart ($T_{ox} = 1300$ K, $P_{red} = 10^{-4}$ bar, $\alpha = 0.95$, $\varepsilon_{gg} = 0$, $P_{c,in} = 75$ bar, and $P_{t,in} = 200$ bar).

The effect of ascension in the T_{red} on the η_{fuel}, η_{W_t}, and η_{en} of the system are presented in Figure 4a. Based on the substantial loss in the $\dot{Q}_{solar}$ and the increment in the conversion rate, the trend of η_{fuel} was similar to that of $\dot{Q}_{red}$. In terms of numbers, the highest $\eta_{fuel} = 11\%$ in the cycle was obtained at $T_{red} = 2000$ K. Due to the ascension of the conversion rate, a higher quantity of CO was released during the oxidation reaction, reducing the amount of CO_2 which was delivered into the turbine. The η_{W_t}, thus, dropped from 7.8% to

1.9% when T_{red} upsurged from 1400–2100 K. According to Equation (31), the η_{en} rose to 13.8%, as T_{red} increased from 1400–1900 K and decreased by 1.4% when T_{red} rose to 2100 K.

3.3. Oxidation Temperature

After investigating the influence of T_{red}, this part further explores the consequence of a rise in T_{ox} from 700–1500 K on energy distribution associated with the cycle. The energy trend of each part is reported in Figure 5b at constant T_{red} = 1900 K and ε_{gg} = 0.9 (at stable P_{red} = 10^{-4} bar). According to Equation (9), the η_{th} was stable when T_{red} was a constant.
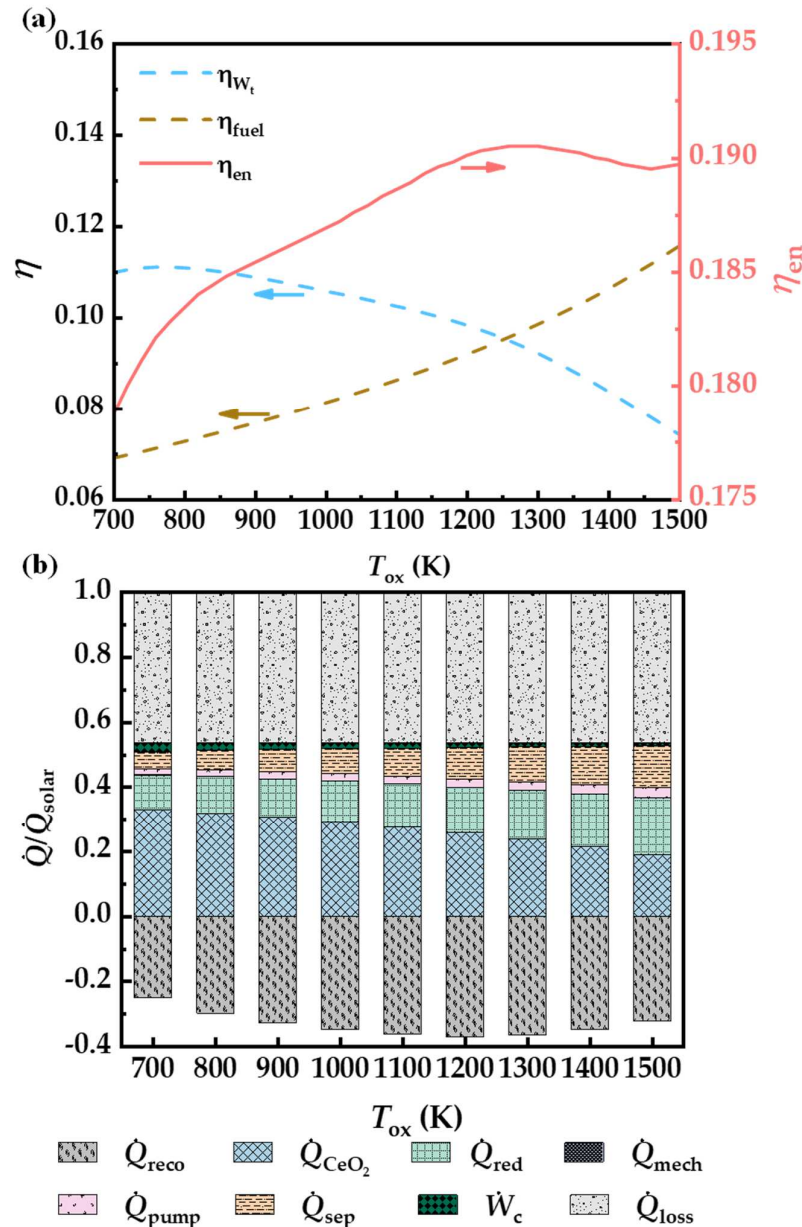
Figure 5. (a) Effect of T_{ox} on η_{fuel}, η_{W_t}, and η_{en} (P_{red} = 10^{-4} bar), (b) energy balance chart (T_{red} = 1900 K, P_{red} = 10^{-4} bar, α = 0.95, ε_{gg} = 0.9, $P_{c,in}$ = 75 bar, and $P_{t,in}$ = 200 bar).

Namely, the percentage of $\dot{Q}_{loss}$ was maintained at 0.46 due to the fixed thermodynamic efficiency. In the case of the solar receiver, the inlet and outlet of ceria was T_{ox} and T_{red}, individually. Thus, while the T_{ox} was increased, the temperature gap between the inlet and outlet ceria temperature was diminished. This decrease in the temperature gap resulted in an upturn in the $\dot{Q}_{red}$, as a higher quantity of cerium dioxide can be heated to the reduction temperature. Conversely, the ratio of the $\dot{Q}_{CeO_2}$ diminished from 1220–828.3 kW when the T_{ox} increased from 700–1500 K. This consequence was caused by the upsurged $\dot{Q}_{pump}$ and $\dot{Q}_{sep}$ because more O_2 and CO was released with the increase of the ceria. For instance, the proportion of $\dot{Q}_{pump}$ and $\dot{Q}_{sep}$ rose by 0.01 and 0.07, respectively, due to the upsurge in the T_{ox} from 700 to 1500 K.

The η_{fuel}, η_{W_t}, and η_{en} were calculated as functions of T_{ox}, meanwhile, the results are presented in Figure 5a. The finding shown in the figure indicates that the η_{fuel} had a continuous growth due to the increased $\dot{Q}_{red}$. In terms of numbers, the η_{fuel} rose from 6.9–11.6% when the T_{ox} increased from 700–1500 K. The upturned $\dot{Q}_{red}$ resulted in the reduction of $\dot{Q}_{CeO_2}$, diminishing the quantity of CO_2 imported into the turbine. The η_{W_t}, thus, reduced from 11.1–7.4%, as the T_{ox} upsurged from 760–1500 K. It should be noted that there was an ascension of the η_{W_t} with the increment of T_{ox} because the enthalpy of CO_2 increases rapidly during this period. The trend of η_{en} about T_{red} is similar to that about T_{ox}. The highest $\eta_{en} = 19.05\%$ in this case was obtained at $T_{ox} = 1300$ K, and the η_{en} upsurged from 18.95–18.87% with the increment of the T_{ox} from 1460–1500 K due to the considerable rise in the η_{fuel}.

3.4. Heat Recovery

At $T_{red} = 1900$ K and $T_{ox} = 1300$ K, the effect of variation in the ε_{gg} from 0 to 1 on the η_{en} was investigated. In case of the heat exchanger, as the ε_{gg} was increased, the $\dot{Q}_{reco}$ and the quantity of CO_2 upsurged due to the constant $\dot{Q}_{rec}$. Figure 6a indicates that the $\dot{Q}_{reco}$ had an ascension from 0 to 2140 kW when the ε_{gg} increased from 0 to 1. The consequence of the increment in the ε_{gg} for the $\dot{Q}_{sep}$ and $\dot{Q}_{solar}$ was explored using Equations (25) and (27), respectively. With the increment in the ε_{gg} from 0 to 1, the $\dot{Q}_{sep}$ was enhanced from 333.6–470.3 kW. This ascension in the $\dot{Q}_{sep}$ reflected an increase in the $\dot{Q}_{solar}$ from 3870–4210 kW.

Figure 6b represents the variation associated with the η_{fuel}, η_{W_t}, and η_{en} as a function of ε_{gg}. Because the $\dot{Q}_{rec}$ was at a constant and the ceria can be converted completely, the value of $\dot{n}_{CO}HHV$ was kept at 406.9 kW. As previously studied, the $\dot{Q}_{solar}$ was escalated with the increment in the ε_{gg}. The η_{fuel}, thus, diminished from 10.5–9.7% when the ε_{gg} increased from 0 to 1. In contrast, the η_{W_t} upsurged from 3.2–11.6%, as a larger amount of CO_2 was fed into the turbine. Overall, the η_{en} improved by 7.5%, as calculated via Equation (31).

(a)

(b)
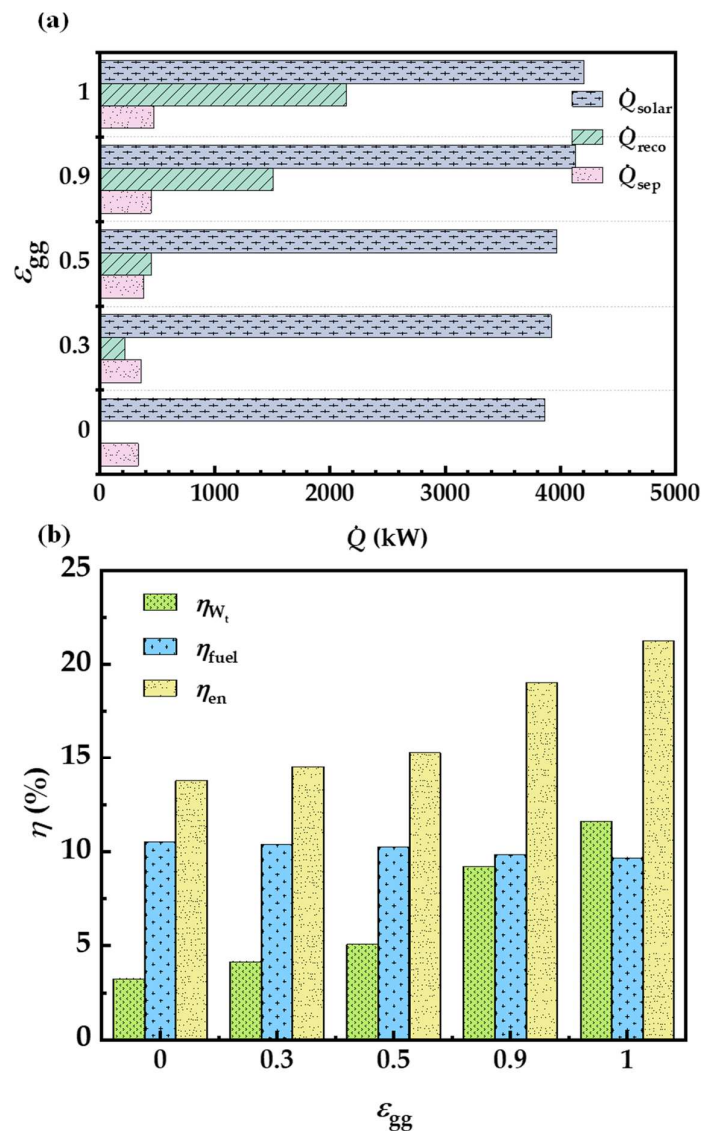
Figure 6. (**a**) Effect of ε_{gg} on $\dot{Q}_{solar}$, $\dot{Q}_{reco}$, and $\dot{Q}_{sep}$, (**b**) effect of ε_{gg} on η_{fuel}, η_{W_t}, and η_{en} (T_{red} = 1900 K, T_{ox} = 1300 K, P_{red} = 10^{-4} bar, α = 0.95, $P_{c,in}$ = 75 bar, and $P_{t,in}$ = 200 bar).

3.5. Cycle High Pressure

The effect of upswing in the cycle high pressure (i.e., $P_{t,in}$) on the $\dot{n}_{CO_2}$ and $\dot{W}_t$ of the cycle is presented in Figure 7b, when T_{red} = 1900 K, T_{ox} = 1300 K, and ε_{gg} = 0.9.

In case of the compressor, the inlet and the outlet pressure of CO_2 was 75 bar and $P_{t,in}$, respectively. Hence, as the $P_{t,in}$ was increased, the pressure gap between the inlet and the outlet of the compressor upsurged. Thus, the outlet temperature of the compressor rose accordingly by about a dozen degrees, reducing the temperature increase required for CO_2. However, Figure 8 indicates that the average heat capacity of CO_2 was increased due to the increment in the $P_{t,in}$. Thus, the $\dot{n}_{CO_2}$ had a decrease with the upturned $P_{t,in}$. In terms of numbers, the $\dot{n}_{CO_2}$ diminished from 45.5–33.9 mol/s, as the $P_{t,in}$ improved from 180–260 bar. In addition, the $h_{t,in}$ can be reduced due to the ascension in the $P_{t,in}$, making it possible for the turbine to export more power under a limited flow rate. Thence, the highest $\dot{W}_t$ = 437.9 kJ/s in case of the cycle was obtained at $P_{t,in}$ = 260 bar, reaching to the maximum value, which was 10.6%, and then diminished in the range of 260–300 bar. Opposite to this consequence, the η_{fuel} remained at about 9.8% due to the stable CO generation and $\dot{Q}_{solar}$. Overall, it seems that the oscillation of the system high pressure mainly impacted the η_{en}

when T_{red} and T_{ox} were constant, as the trend of η_{en} was similar to that of η_{W_t}. In terms of values, the maximum $\eta_{en} = 20.4\%$ was attained at $P_{t,in} = 260$ bar.
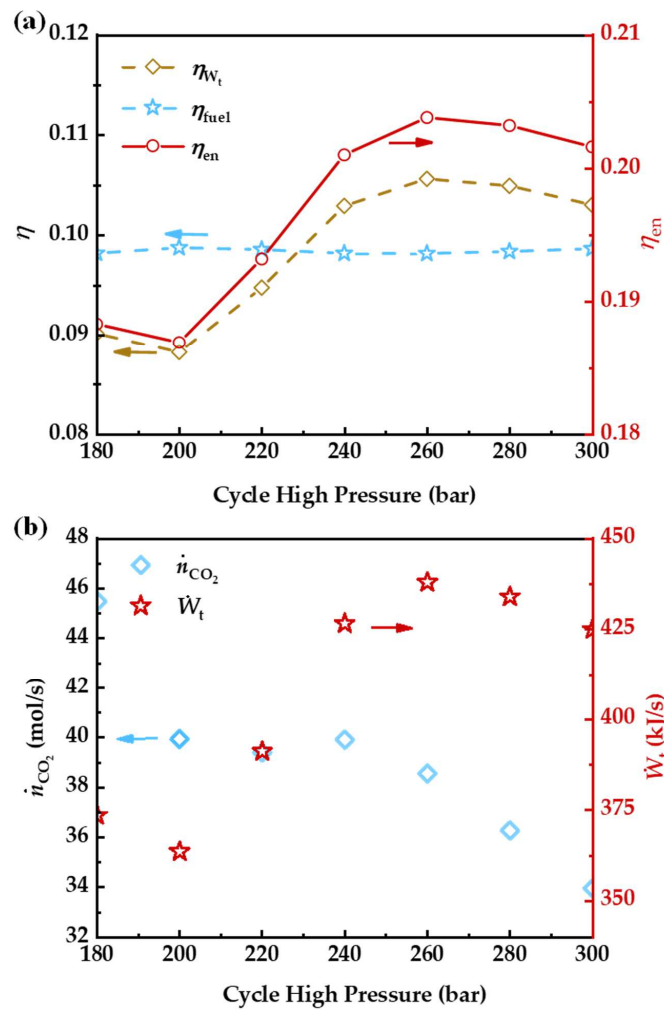
Figure 7. (**a**) Effect of cycle high pressure on η_{fuel}, η_{W_t}, and η_{en} ($P_{red} = 10^{-4}$ bar), (**b**) influence of cycle high pressure on $\dot{n}_{CO_2}$ and $\dot{W}_t$ ($T_{red} = 1900$ K, $T_{ox} = 1300$ K, $P_{red} = 10^{-4}$ bar, $\alpha = 0.95$, $\varepsilon_{gg} = 0.9$, $P_{c,in} = 75$ bar).
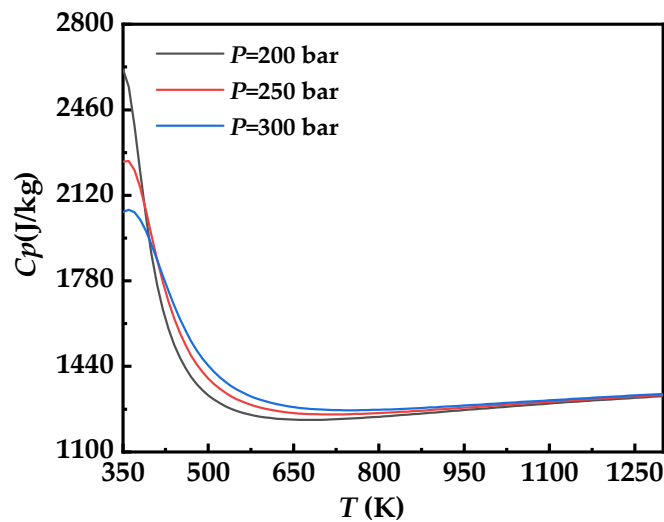
Figure 8. Effect of temperature on supercritical CO_2 heat capacity.

3.6. Cycle Low Pressure

Figure 9a presents the effect of cycle low pressure (i.e., $P_{c,in}$) on system performance. It can be seen that the increasing cycle low pressure was profitless in terms of both η_{W_t} and η_{en} in the range of 75–87 bar, but the η_{fuel} was maintained at 9.9%, as the increase in cycle low pressure caused the compressor outlet temperature to decrease. However, unlike the cycle high pressure, the increase in cycle low pressure from 72 bar to 90 bar will decrease the compressor outlet temperature by 50 degrees. Near the critical point of supercritical CO_2, a temperature difference of a few tens of degrees will cause a wide range of fluctuations in the heat capacity of supercritical CO_2. In addition, the average heat capacity of supercritical CO_2 was upsurged with the increment in cycle low pressure. Therefore, as shown in Figure 9b, our calculated CO_2 flow rate and $\dot{W}_t$ are not regular with the change of cycle low pressure.
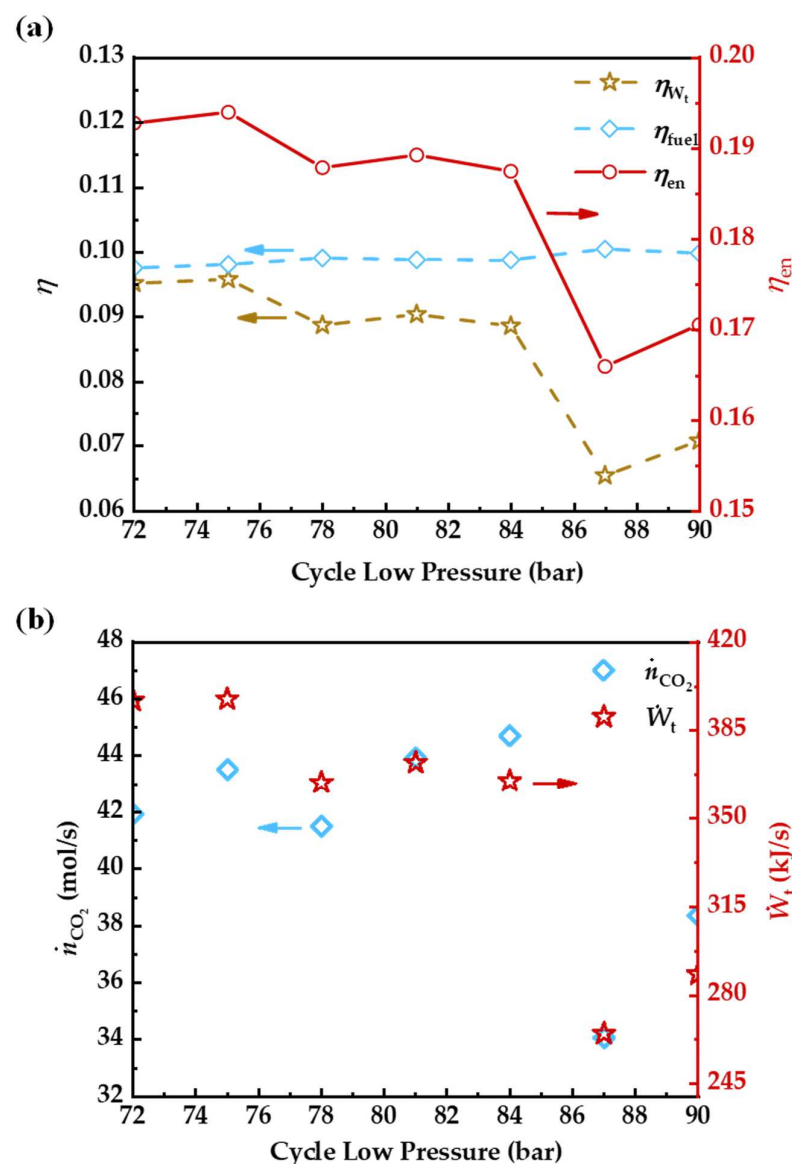
Figure 9. (**a**) Effect of cycle low pressure on η_{fuel}, η_{W_t}, and η_{en} ($P_{red} = 10^{-4}$ bar), (**b**) influence of cycle low pressure on $\dot{n}_{CO_2}$ and $\dot{W}_t$ ($T_{red} = 1900$ K, $T_{ox} = 1300$ K, $P_{red} = 10^{-4}$ bar, $\alpha = 0.95$, $\varepsilon_{gg} = 0.9$, $P_{t,in} = 200$ bar).

3.7. Economic Analysis

The economic evaluation can derive the production cost of solar thermal chemical CO production and electricity generation [55,56]. This cost takes into account the time value cost of money and calculates the total cost of the system over its life cycle [57,58]. Using the annual rate method to derive annualized values, the total life cycle cost (*TLCC*) can be used to derive the cost per kilogram of CO. *TLCC* is computed by Equation (32), wherein *V* denotes the investments, *M* the tax rate, PV_{DEP} the present value of the series of occurring depreciation, and $PV_{O\&M}$ the present value of operation and maintenance costs. And the present value of reducing recurring *U* over a time period is found with Equation (33). In case of constant annual payments, the equation can be simplified using the annuity factor $N = i \left(1 - (1+i)^{-b}\right)^{-1}$, wherein *i* is the interest rate and *b* is the lifetime of the system.

$$TLCC = \frac{V - (M * PV_{DEP}) + (1 - M)\, PV_{O\&M}}{1 - M} \tag{32}$$

$$PV_x = \{DEP, O\&M\} = \sum_{j=1}^{U_j} \frac{U_j}{(1+i)^j} = U_j * N \tag{33}$$

The production costs, or levelized costs per kilogram of CO (*LCO*), can then be determined by dividing the *TLCC* by the annual factor times the annual production rate *Q* (kg CO per year): $LCO = \frac{TLCC}{Q*N}$. Finally, Equation (32) can be simplified to $TLCC = V + PV_{O\&M}$, when the project is supported by the government and no taxes have to be paid.

Regardless of weather changes and the intensity of light, the system's working time is set to 12 h a day, and a year is 365 days. At the highest energy conversion efficiency, the value of the annual output of CO is 634,819.68 kg, while the annual output of electricity is 76,734.97 kWh. The lifetime of the system is 25 years, the average interest rate is 6%, and other parameters are obtained from the previous literature [59,60]. According to Equations (32) and (33), the unit cost of solar fuel is $ 5.86/kg, which is lower than the average market price of CO. The unit cost further decreases to $ 5.62/kg when economic benefits of electricity generation are deducted. The electricity produced by the supercritical CO_2 cycle reduces the cost of the conventional thermochemical cycle by 4%, improving the economics of the system.

4. Conclusions

In summary, we proposed an alternative way to upsurge energy conversion efficiency by integrating solar thermochemical CO_2 splitting with a supercritical CO_2 thermodynamic cycle. For a traditional thermochemical CO_2 splitting cycle, the optimal reduction temperature is around 1900 K at a partial pressure of oxygen of 10^{-4} bar, where the highest energy conversion efficiency is 11%. For an integrated system, the optimal reduction and oxidation temperatures were found to be 1900 and 1300 K, respectively. Simultaneously, the fuel efficiency was constant at 9.8% and the energy efficiency was upturned to 20.4% under the cycle high pressure of 260 bar. The superior performance is attributed to efficient harvesting of waste heat and synergy of CO_2 splitting cycles with supercritical CO_2 cycles. This work provides alternative routes for improving low efficiency of traditional solar thermochemical CO_2 splitting cycles while also enriching products beyond single fuels.

Institutional Review Board Statement: Not applicable.

Informed Consent Statement: Not applicable.

Data Availability Statement: Not applicable.

Conflicts of Interest: The authors declare no conflict of interest.

Nomenclature

A	area (m^{-2})
C	solar concentration
Cp	specific heat capacity ($J\,mol^{-1}\,K^{-1}$)
Fr	view factor
h	specific enthalpy (kJ/mol) or heat transfer coefficient ($W\,m^{-2}\,K^{-1}$)
H	height (m)
HHV	high heating value (kJ/mol)
I	solar radiation intensity (kW/m^2)
$\dot{n}$	mole flow rate (mol/s)
P	pressure (bar)
$\dot{Q}$	heat rate (kW)
R	universal gas constant
T	temperature (K)
$\dot{W}$	work rate (kW)

Greek

α	fraction completed for oxidation reaction
δ	non-stoichiometric coefficient
$\Delta\delta$	non-stoichiometric coefficient difference
ΔH	change in enthalpy or
ΔS	change in entropy
ε	emissivity or heat recovery effectiveness
η	efficiency
ρ	reflectivity

Subscripts

0	ambient
1,2, . . .	state point
abs	absorb
ape	aperture
c	compressor
conv	convection
en	energy
g	gas
hox	heat in exothermic oxidation reaction
in	inlet
mech	mechanically moving objects
out	outlet
ox	oxidation
pump	vacuum pump
rad	radiation
rec	receiver
reco	recovery
red	reduction
ref	reflection
sep	separation
surf	surface
t	turbine
tc	total
th	thermodynamic

References

1.　NOAA Administration. Carbon Dioxide Now More Than 50% Higher Than Pre-Industrial Levels. Available online: www.noaa.gov (accessed on 11 July 2022).

2.　Haeussler, A.; Abanades, S.; Julbe, A.; Jouannaux, J.; Drobek, M.; Ayral, A.; Cartoixa, B. Remarkable performance of microstructured ceria foams for thermochemical splitting of H2O and CO2 in a novel high–temperature solar reactor. *Chem. Eng. Res. Des.* **2020**, *156*, 311–323. [CrossRef]

3.　Zang, G.; Sun, P.; Elgowainy, A.A.; Bafana, A.; Wang, M. Performance and cost analysis of liquid fuel production from H$_2$ and CO$_2$ based on the Fischer-Tropsch process. *J. CO2 Util.* **2021**, *46*, 101459. [CrossRef]

4.　Gong, W.; Ye, R.-P.; Ding, J.; Wang, T.; Shi, X.; Russell, C.K.; Tang, J.; Eddings, E.G.; Zhang, Y.; Fan, M. Effect of copper on highly effective Fe-Mn based catalysts during production of light olefins via Fischer-Tropsch process with low CO$_2$ emission. *Appl. Catal. B Environ.* **2020**, *278*, 119302. [CrossRef]

5.　Sonal; Ahmad, E.; Upadhyayula, S.; Pant, K.K. Biomass-derived CO$_2$ rich syngas conversion to higher hydrocarbon via Fischer-Tropsch process over Fe–Co bimetallic catalyst. *Int. J. Hydrog. Energy* **2019**, *44*, 27741–27748. [CrossRef]

6.　Li, D.; Kassymova, M.; Cai, X.; Zang, S.-Q.; Jiang, H.-L. Photocatalytic CO$_2$ reduction over metal-organic framework-based materials. *Coord. Chem. Rev.* **2020**, *412*, 213262. [CrossRef]

7.　Xiong, X.; Mao, C.; Yang, Z.; Zhang, Q.; Waterhouse GI, N.; Gu, L.; Zhang, T. Photocatalytic CO$_2$ Reduction to CO over Ni Single Atoms Supported on Defect-Rich Zirconia. *Adv. Energy Mater.* **2020**, *10*, 2002928. [CrossRef]

8.　Chen, Z.; Hu, Y.; Wang, J.; Shen, Q.; Zhang, Y.; Ding, C.; Bai, Y.; Jiang, G.; Li, Z.; Gaponik, N. Boosting Photocatalytic CO2 Reduction on CsPbBr3 Perovskite Nanocrystals by Immobilizing Metal Complexes. *Chem. Mater.* **2020**, *32*, 1517–1525. [CrossRef]

9.　Huan, T.N.; Corte DA, D.; Lamaison, S.; Karapinar, D.; Lutz, L.; Menguy, N.; Foldyna, M.; Turren-Cruz, S.-H.; Hagfeldt, A.; Bella, F.; et al. Low-cost high-efficiency system for solar-driven conversion of CO2 to hydrocarbons. *Proc. Natl. Acad. Sci. USA* **2019**, *116*, 9735–9740. [CrossRef]

10.　Sriramagiri, G.M.; Ahmed, N.; Luc, W.; Dobson, K.D.; Hegedus, S.S.; Jiao, F. Toward a Practical Solar-Driven CO$_2$ Flow Cell Electrolyzer: Design and Optimization. *ACS Sustain. Chem. Eng.* **2017**, *5*, 10959–10966. [CrossRef]

11.　Küngas, R. Review—Electrochemical CO$_2$ Reduction for CO Production: Comparison of Low- and High-Temperature Electrolysis Technologies. *J. Electrochem. Soc.* **2020**, *167*, 044508. [CrossRef]

12.　Chen, Z.; Jiang, Q.; An, H.; Zhang, J.; Hao, S.; Li, X.; Cai, L.; Yu, W.; You, K.; Zhu, X.; et al. Platinum Group Metal Catalyst (RuOx, PtOx, and IrOx)-Decorated Ceria-Zirconia Solid Solution as High Active Oxygen Carriers for Solar Thermochemical CO$_2$ Splitting. *ACS Catal.* **2022**, *12*, 7719–7736. [CrossRef]

13.　Riaz, A.; Kreider, P.; Kremer, F.; Tabassum, H.; Yeoh, J.S.; Lipiński, W.; Lowe, A. Electrospun Manganese-Based Perovskites as Efficient Oxygen Exchange Redox Materials for Improved Solar Thermochemical CO2 Splitting. *ACS Appl. Energy Mater.* **2019**, *2*, 2494–2505. [CrossRef]

14.　Liu, X.; Wang, T.; Gao, K.; Meng, X.; Xu, Q.; Song, C.; Zhu, Z.; Zheng, H.; Hao, Y.; Xuan, Y. Ca- and Ga-Doped LaMnO3 for Solar Thermochemical CO2 Splitting with High Fuel Yield and Cycle Stability. *ACS Appl. Energy Mater.* **2021**, *4*, 9000–9012. [CrossRef]

15.　Lu, Y.; Zhu, L.; Agrafiotis, C.; Vieten, J.; Roeb, M.; Sattler, C. Solar fuels production: Two-step thermochemical cycles with cerium-based oxides. *Prog. Energy Combust. Sci.* **2019**, *75*, 100785. [CrossRef]

16.　Xiao, L.; Wu, S.-Y.; Li, Y.-R. Advances in solar hydrogen production via two-step water-splitting thermochemical cycles based on metal redox reactions. *Renew. Energy* **2012**, *41*, 1–12. [CrossRef]

17.　Kodama, T.; Gokon, N. Thermochemical Cycles for High-Temperature Solar Hydrogen Production. *Chem. Rev.* **2007**, *107*, 4048–4077. [CrossRef]

18.　Yutaka, N.; Bernard, C. Production of Carbon Monoxide by Direct Thermal Splitting of Carbon Dioxide at High Temperature. *Bull. Chem. Soc. Jpn.* **1986**, *59*, 1997–2002.

19.　Smestad, G.P.; Steinfeld, A. Review: Photochemical and Thermochemical Production of Solar Fuels from H2O and CO2 Using Metal Oxide Catalysts. *Ind. Eng. Chem. Res.* **2012**, *51*, 11828–11840. [CrossRef]

20.　Kang, Y.; Han, Y.; Wei, C.; Liu, K.; Tian, M.; Huang, C.; Wang, C.; Lin, J.; Hou, B.; Pan, X.; et al. A novel carbon cycle process assisted by Ni/La2O3 catalyst for enhanced thermochemical CO$_2$ splitting. *J. Energy Chem.* **2021**, *61*, 297–303. [CrossRef]

21.　Kong, H.; Kong, X.; Wang, H.; Wang, J. A strategy for optimizing efficiencies of solar thermochemical fuel production based on nonstoichiometric oxides. *Int. J. Hydrog. Energy* **2019**, *44*, 19585–19594. [CrossRef]

22.　Muhich, C.L.; Blaser, S.; Hoes, M.C.; Steinfeld, A. Comparing the solar-to-fuel energy conversion efficiency of ceria and perovskite based thermochemical redox cycles for splitting H2O and CO2. *Int. J. Hydrog. Energy* **2018**, *43*, 18814–18831. [CrossRef]

23.　Panlener, R.J.; Blumenthal, R.N.; Garnier, J.E. A thermodynamic study of nonstoichiometric cerium dioxide. *J. Phys. Chem. Solids* **1975**, *36*, 1213–1222. [CrossRef]

24.　Le Gal, A.; Abanades, S.; Flamant, G. CO2 and H2O Splitting for Thermochemical Production of Solar Fuels Using Nonstoichiometric Ceria and Ceria/Zirconia Solid Solutions. *Energy Fuels* **2011**, *25*, 4836–4845. [CrossRef]

25.　Zhu, L.; Lu, Y.; Li, F. Reactivity of Ni, Cr and Zr doped ceria in CO$_2$ splitting for CO production via two-step thermochemical cycle. *Int. J. Hydrog. Energy* **2018**, *43*, 13754–13763. [CrossRef]

26.　Zhu, L.; Lu, Y. Reactivity and Efficiency of Ceria-Based Oxides for Solar CO$_2$ Splitting via Isothermal and Near-Isothermal Cycles. *Energy Fuels* **2018**, *32*, 736–746. [CrossRef]

27. Gao, K.; Liu, X.; Jiang, Z.; Zheng, H.; Song, C.; Wang, X.; Tian, C.; Dang, C.; Sun, N.; Xuan, Y. Direct solar thermochemical CO_2 splitting based on Ca- and Al- doped $SmMnO_3$ perovskites: Ultrahigh CO yield within small temperature swing. *Renew. Energy* **2022**, *194*, 482–494. [CrossRef]

28. Kaneko, H.; Miura, T.; Fuse, A.; Ishihara, H.; Taku, S.; Fukuzumi, H.; Naganuma, Y.; Tamaura, Y. Rotary-Type Solar Reactor for Solar Hydrogen Production with Two-step Water Splitting Process. *Energy Fuels* **2007**, *21*, 2287–2293. [CrossRef]

29. Johnson, T.A.; Hogan, J.; Roy, E.; McDaniel, A.H.; Siegel, N.P.; Dedrick, D.E.; Stechel, E.B.; Diver, J.; Richard, B.; Miller, J.E.; et al. *Reimagining Liquid Transportation Fuels: Sunshine to Petrol*; Sandia National Laboratories (SNL): Albuquerque, NM, USA; Livermore, CA, USA, 2012; p. 33.

30. Marxer, D.; Furler, P.; Scheffe, J.; Geerlings, H.; Falter, C.; Batteiger, V.; Sizmann, A.; Steinfeld, A. Demonstration of the Entire Production Chain to Renewable Kerosene via Solar Thermochemical Splitting of H_2O and CO_2. *Energy Fuels* **2015**, *29*, 3241–3250. [CrossRef]

31. Farsi, A.; Dincer, I. Thermodynamic assessment of a hybrid particle-based concentrated solar power plant using fluidized bed heat exchanger. *Sol. Energy* **2019**, *179*, 236–248. [CrossRef]

32. Alqahtani, B.J.; Patiño-Echeverri, D. Integrated Solar Combined Cycle Power Plants: Paving the way for thermal solar. *Appl. Energy* **2016**, *169*, 927–936. [CrossRef]

33. Wang, K.; He, Y.-L. Thermodynamic analysis and optimization of a molten salt solar power tower integrated with a recompression supercritical CO_2 Brayton cycle based on integrated modeling. *Energy Convers. Manag.* **2017**, *135*, 336–350. [CrossRef]

34. Wang, X.; Liu, Q.; Lei, J.; Han, W.; Jin, H. Investigation of thermodynamic performances for two-stage recompression supercritical CO2 Brayton cycle with high temperature thermal energy storage system. *Energy Convers. Manag.* **2018**, *165*, 477–487. [CrossRef]

35. Pitz-Paal, R.; Botero, N.B.; Steinfeld, A. Heliostat field layout optimization for high-temperature solar thermochemical processing. *Sol. Energy* **2011**, *85*, 334–343. [CrossRef]

36. Ehrhart, B.; Gill, D. Evaluation of Annual Efficiencies of High Temperature Central Receiver Concentrated Solar Power Plants with Thermal Energy Storage. *Energy Procedia* **2014**, *49*, 752–761. [CrossRef]

37. Dähler, F.; Wild, M.; Schäppi, R.; Haueter, P.; Cooper, T.; Good, P.; Larrea, C.; Schmitz, M.; Furler, P.; Steinfeld, A. Optical design and experimental characterization of a solar concentrating dish system for fuel production via thermochemical redox cycles. *Sol. Energy* **2018**, *170*, 568–575. [CrossRef]

38. Duffie, J.A.; Beckman, W.A.; Worek, W.M. Solar Engineering of Thermal Processes. *J. Sol. Energy Eng.* **1994**, *116*, 67–68. [CrossRef]

39. Li, X.; Kong, W.; Wang, Z.; Chang, C.; Bai, F. Thermal model and thermodynamic performance of molten salt cavity receiver. *Renew. Energy* **2010**, *35*, 981–988. [CrossRef]

40. Ho, C.K.; Christian, J.M.; Yellowhair, J.; Armijo, K.; Kolb, W.J.; Jeter, S.; Golob, M.; Nguyen, C. Performance evaluation of a high-temperature falling particle receiver. In *Energy Sustainability*; ASME: New York, NY, USA, 2016.

41. Liu, Y.; Wang, Y.; Huang, D. Supercritical CO2 Brayton cycle: A state-of-the-art review. *Energy* **2019**, *189*, 115900. [CrossRef]

42. Xu, C.; Wang, Z.; Li, X.; Sun, F. Energy and exergy analysis of solar power tower plants. *Appl. Therm. Eng.* **2011**, *31*, 3904–3913. [CrossRef]

43. Zinkevich, M.; Djurovic, D.; Aldinger, F. Thermodynamic modelling of the cerium–oxygen system. *Solid State Ion.* **2006**, *177*, 989–1001. [CrossRef]

44. Bulfin, B.; Lowe, A.J.; Keogh, K.A.; Murphy, B.E.; Lübben, O.; Krasnikov, S.A.; Shvets, I.V. Analytical Model of CeO_2 Oxidation and Reduction. *J. Phys. Chem. C* **2013**, *117*, 24129–24137. [CrossRef]

45. Bader, R.; Venstrom, L.J.; Davidson, J.H.; Lipiński, W. Thermodynamic Analysis of Isothermal Redox Cycling of Ceria for Solar Fuel Production. *Energy Fuels* **2013**, *27*, 5533–5544. [CrossRef]

46. Bulfin, B.; Call, F.; Lange, M.; Lübben, O.; Sattler, C.; Pitz-Paal, R.; Shvets, I.V. Thermodynamics of CeO_2 Thermochemical Fuel Production. *Energy Fuels* **2015**, *29*, 1001–1009. [CrossRef]

47. Bulfin, B.; Lange, M.; de Oliveira, L.; Roeb, M.; Sattler, C. Solar thermochemical hydrogen production using ceria zirconia solid solutions: Efficiency analysis. *Int. J. Hydrog. Energy* **2016**, *41*, 19320–19328. [CrossRef]

48. Ricken, M.; Nölting, J.; Riess, I. Specific heat and phase diagram of nonstoichiometric ceria (CeO_{2-x}). *J. Solid State Chem.* **1984**, *54*, 89–99. [CrossRef]

49. Guo, J. Design analysis of supercritical carbon dioxide recuperator. *Appl. Energy* **2016**, *164*, 21–27. [CrossRef]

50. PraveenKumar, S.; Agyekum, E.B.; Velkin, V.I.; Yaqoob, S.J.; Adebayo, T.S. Thermal management of solar photovoltaic module to enhance output performance: An experimental passive cooling approach using discontinuous aluminum heat sink. *Int. J. Renew. Energy Res.* **2021**, *11*, 1700–1712.

51. Ma, Z.; Glatzmaier, G.C.; Mehos, M. Development of Solid Particle Thermal Energy Storage for Concentrating Solar Power Plants that Use Fluidized Bed Technology. *Energy Procedia* **2014**, *49*, 898–907. [CrossRef]

52. Shimizu, A.; Yokomine, T.; Nagafuchi, T. Development of gas–solid direct contact heat exchanger by use of axial flow cyclone. *Int. J. Heat Mass Transf.* **2004**, *47*, 4601–4614. [CrossRef]

53. Ma, Z.; Martinek, J. Analysis of a Fluidized-Bed Particle/Supercritical-CO2 Heat Exchanger in a Concentrating Solar Power System. *J. Sol. Energy Eng.* **2020**, *143*, 031010. [CrossRef]

54. Lin, M.; Haussener, S. Solar fuel processing efficiency for ceria redox cycling using alternative oxygen partial pressure reduction methods. *Energy* **2015**, *88*, 667–679. [CrossRef]

55. Baloch, A.A.B.; Bahaidarah, H.M.S.; Gandhidasan, P.; Al-Sulaiman, F.A. Experimental and numerical performance analysis of a converging channel heat exchanger for PV cooling. *Energy Convers. Manag.* **2015**, *103*, 14–27. [CrossRef]
56. Praveenkumar, S.; Gulakhmadov, A.; Agyekum, E.B.; Alwan, N.T.; Velkin, V.I.; Sharipov, P.; Safaraliev, M.; Chen, X. Experimental Study on Performance Enhancement of a Photovoltaic Module Incorporated with CPU Heat Pipe—A 5E Analysis. *Sensors* **2022**, *22*, 6367. [CrossRef]
57. Agyekum, E.B.; PraveenKumar, S.; Alwan, N.T.; Velkin, V.I.; Shcheklein, S.E.; Yaqoob, S.J. Experimental Investigation of the Effect of a Combination of Active and Passive Cooling Mechanism on the Thermal Characteristics and Efficiency of Solar PV Module. *Inventions* **2021**, *6*, 63. [CrossRef]
58. Agyekum, E.B.; PraveenKumar, S.; Alwan, N.T.; Velkin, V.I.; Adebayo, T.S. Experimental Study on Performance Enhancement of a Photovoltaic Module Using a Combination of Phase Change Material and Aluminum Fins—Exergy, Energy and Economic (3E) Analysis. *Inventions* **2021**, *6*, 69. [CrossRef]
59. Falter, C.; Sizmann, A. Solar Thermochemical Hydrogen Production in the USA. *Sustainability* **2021**, *13*, 7804. [CrossRef]
60. Yang, J.; Yang, Z.; Duan, Y. Load matching and techno-economic analysis of CSP plant with S–CO_2 Brayton cycle in CSP-PV-wind hybrid system. *Energy* **2021**, *223*, 120016. [CrossRef]